Characterization of acousto-optical interaction in planar silica optical waveguide by the finite element method

B. M. A. RAHMAN[1,*] AND M. M. RAHMAN[1]

[1] Department of Electrical and Electronic Engineering,City University London,, Northampton Square, London, EC1V 0HB, UK
[*] Corresponding author: B.M.A.Rahman@city.ac.uk

Compiled March 7, 2016

A full-vectorial finite element based approach is used to find accurate modal solutions for the acoustic modes in a Ge-doped planar silica optical waveguide. To enhance the accuracy of the solution, the existing structural symmetry is exploited and rigorous analyses of the interactions between the guided acoustic and optical modes are performed. The Stimulated Brillouin Scattering (SBS) frequency and the overlaps between the fundamental and the higher order transverse and longitudinal acoustic modes and the fundamental quasi-TE optical mode are presented.

OCIS codes: *(130.2790) Guided waves; (170.1065) Acousto-optics; (230.7390) Waveguides, planar; (290.5900) Scattering, stimulated Brillouin.*

http://dx.doi.org/10.1364/aop.XX.XXXXXX

1. INTRODUCTION

Stimulated Brillouin scattering (SBS) is a nonlinear process that takes place in an optical fiber when the optical intensity is high. This intense light beam while propagating through an optical fiber produces an acoustic vibration in the fiber material due to its large electric field, through the process known as electrostriction. This phenomenon produces density fluctuations in the fiber medium, which modulates the linear refractive index of the medium and results in an electrostrictive-nonlinearity [1]. This modulated refractive index behaves as an index grating and Stokes waves are generated as a result and the further beating of the Stokes and the pump waves stimulates the Brillouin scattering (SBS).

Silica optical fibers are the most extensively used optical waveguides due to their extremely low optical loss and wide availability. Although, the advantage of this wide available bandwidth of the optical fibers can be fully exploited by multiplexing several channels in the same fiber, however generation of the Stokes signal can limit higher power delivery if the channel widths are narrow [2], and more specifically for higher power delivery for material processing and defence applications. In addition, SBS can be exploited for development of novel distributed optical sensors.

Acoustic waves can be associated with the material properties such as density, elasticity, Young's modulus, and Poisson's ratio [3]. The propagation of acoustic waves is associated with the displacement of the particles of the waveguide materials along the longitudinal direction and in the transverse plane. The analyses of the acousto-optical interactions are generally complex, especially for those waveguides with a strong material contrast or with more complex shapes, such as micro-structured optical fibers [4] and sub-wavelength waveguides, such as silicon nanowires. Modes in acoustic waveguides are more complex in nature and have been traditionally categorized as torsional, bending, rotational or longitudinal [5, 6] type. However, the modes in acoustic waveguides with two-dimensional confinement are also hybrid in nature [7], and these are similar to the optical modes in optical waveguides [8]. When the dominant displacement vector is in the transverse plane (either U_X or U_Y) then this mode can be identified as quasi-transverse mode and when U_Z is the dominant displacement vector then this can be identified as quasi-longitudinal modes. However, for simplicity, in this work they are referred as transverse or longitudinal modes. Although, the optical materials are considered mostly to be isotropic (except for some familiar materials such as lithium niobate), but most of the acoustic materials, however, have very different longitudinal and shear wave velocities, and hence, they can be considered as having anisotropic acoustic indices. For such cases, a rigorous full-vectorial analysis [9–11] is necessary for the accurate characterization of their acoustic wave propagation properties.

In this work, a numerical approach, based on the powerful and versatile Finite Element Method (FEM) is used [8, 12, 13]. Thus in this paper, the SBS frequency shifts and the overlaps between the quasi-TE optical mode and both fundamental and higher order transverse and longitudinal acoustic modes are studied extensively for a Ge-doped planar silica waveguide.

2. THEORY

In this paper, the propagation of an acoustic wave is considered along the axial direction of the z-axis. The molecular displacement, U_i, caused due to the propagation of acoustic wave can be represented by a time harmonic wave by [10]:

$$\mathbf{U}_i = \mathbf{u}(u_x, u_y, ju_z)exp[j(\omega t - kz)] \quad (1)$$

where the time dependence of the displacement equation is represented by the angular frequency, ω; the axial dependence of acoustic wave is represented by the propagation constant, k, and u_x, u_y and u_z represent the particle displacement vectors along the x, y and z-axes directions, respectively. As in a lossless waveguide, u_z is 90° out of phase with u_x and u_y, the two transverse components, Eq. (1) can be transformed into a much simpler real eigenvalue equation by simply defining the longitudinal component, u_z, as an imaginary component. The deformation in an acoustically vibrating body can be described by the strain field, **S**, which is given by:

$$\mathbf{S} = \nabla \mathbf{u} \quad (2)$$

The stress field, **T**, can define the elastic restoring forces. The inertial and elastic restoring forces in a freely vibrating body can be linked by the translational equation of motion where:

$$\nabla.\mathbf{T} = \rho \frac{\partial^2 \mathbf{u}}{\partial t^2} \quad (3)$$

Eqs. (2) and (3) can be related by Hooke's Law, which basically states the linear proportionality between the stress and strain, by:

$$T_{ij} = c_{ijkl} S_{kl} \quad (4)$$

where the microscopic spring constants, c_{ijkl}, are the elastic stiffness constants. This fourth order tensor obeys the symmetry condition and hence can be replaced by two suffix notations.

Using Eqs. (2) – (4), a wave equation with **u** as the only variable can be formed [6, 10, 11, 13]. To apply the FEM [14] in a solid structure, writing the displacement field, **u**, with the help of the interpolation shape function helps the identification of its spatial derivatives and undertaking the integrations over the elements. The wave equation associated with the acoustic wave propagation can be developed by employing the powerful Galerkin's approach and minimizing the energy functional, allowing a corresponding eigenvalue equation to be formed, which is given as:

$$([A] - \omega^2[B])\mathbf{U} = \mathbf{F} \quad (5)$$

where [A] represents the stiffness matrix and relates to strain energy; the kinetic energy can be related to the mass matrix [B]. For a given propagation constant, k, these matrices can be generated. Here **F** contains the nodal values of the applied forces, but in this case are taken as zero, which are the column vectors. Solving this generalized eigenvalue equation of the system produces the eigenvalue as ω^2, where ω is the acoustic angular frequency and the eigenvector **U**, the displacement vector. From a given input, k, and its corresponding output, ω, the phase velocity of the acoustic wave, v, can be calculated from:

$$v = \omega / k \quad (6)$$

A Ge-doped silica planar waveguide can also guide optical signals. A FEM approach based on the vector **H**-field formulation is used here for the analysis of the optical modes. This approach is one of the most numerically efficient and accurate approaches to obtain the modal field profiles and the propagation constants of the fundamental and higher order quasi-TE and quasi-TM modes. The full-vectorial formulation is based on the minimization of the full **H**-field energy functional [15],

$$\omega_o^2 = \frac{\int \left[(\nabla \times \mathbf{H})^*.\hat{\epsilon}^{-1}(\nabla \times \mathbf{H}) + p(\nabla.\mathbf{H})^*(\nabla.\mathbf{H})\right] dxdy}{\int \mathbf{H}^*.\hat{\mu}\mathbf{H} dxdy} \quad (7)$$

here ω_o^2 is the eigenvalue and ω_o is the angular frequency of the optical wave, **H** is the full-vectorial magnetic field, $*$ represents the complex conjugate transpose, p is the weighing factor for the penalty term to eliminate spurious solutions and $\hat{\epsilon}$ and $\hat{\mu}$ are the permittivity and permeability, respectively. If required radiation pressure can be calculated from the resulting **H**-field.

In an optical waveguide, a guided optical signal can be scattered by the nonlinear interaction between the pump and Stokes fields and an acoustic wave through the SBS process. In such an event, since both the momentum and energy must be conserved, for a given propagation constant, β_o, of an existing optical mode, the propagation constant, k, of an acoustic mode can be found [16] by using,

$$k = 2\beta_o \quad (8)$$

The SBS gain can be calculated from the overlap integral of the optical field with the displacement vector profile, $\mathbf{U}(x,y)$ [17, 18], or with the density variation profile [19]. The density variation profile holds strong correlation with the displacement vector profile and this normalized overlap [17, 18] can be calculated as:

$$\Gamma_{ij} = \frac{\left(\int |H_{im}|^2 u_{jn} dxdy\right)^2}{\int |H_{im}|^4 dxdy \int |u_{jn}|^2 dxdy}; \quad m,n = x,y,z \quad (9)$$

here H_{im} is the m^{th} component of the magnetic field profile (where m may be x, y or z) of the i^{th} optical mode and u_{jn} is the n^{th} component of the acoustic displacement profile (where n may be x, y or z) of the phase matched j^{th} acoustic mode. The SBS gain is directly related to this overlap integral through the elasto-optic coefficient, p_{12}.

3. RESULTS

In a silica planar waveguide, as shown in Fig. 1, the core is doped with 10% Ge to increase the refractive index. This also increases the acoustic index of the core when compared to the undoped silica cladding [20], thus this optical waveguide also confines both longitudinal and transverse acoustic waves. In this paper the acoustic longitudinal and transverse wave velocities and density of the 10% Ge-doped core are taken as V_{LG} = 5509.67 m/s, V_{SG} = 3474 m/s and ρ_G = 2342 kg/m^3, respectively [21, 22]. By contrast, for the un-doped pure silica cladding, these are considered to be V_{LC} = 5933 m/s,V_{SC} = 3764 m/s and ρ_C = 2202 kg/m^3, respectively [21]. As the velocity of the longitudinal and transverse acoustic modes are different, the materials are effectively 'anisotropic' and the resultant acoustic index contrast between core and cladding are also different. In this case if the cladding acoustic index is taken as 1.0, then the core acoustic index would be 1.071 and 1.077 for longitudinal and transverse modes, respectively. The height (H) and width (W) of the core are taken as H = 3 μm and W = 6 μm, respectively, to ensure that optical mode is guided in this waveguide at the operating wavelength (λ_o) of 1550 nm. Although, cladding was infinite

but depending on the modal confinement a fixed dimension was considered to conserve the FEM mashing requirements. Typically these values were taken as 6 μm in the horizontal and vertical directions on each side. Furthermore, 1000 $\times$ 1000 mesh divisions were used in the horizontal and vertical directions which yields 2 million first order triangles. For this waveguide a two-fold symmetry is available, as shown by two dashed lines, and this has been exploited here to obtain better accuracy in their modal solutions for a give computer resource.

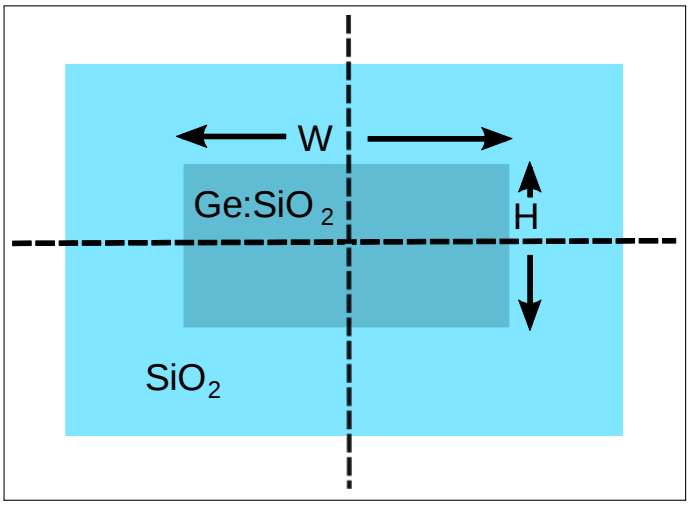

Fig. 1. Ge-doped silica planar optical waveguide structure.

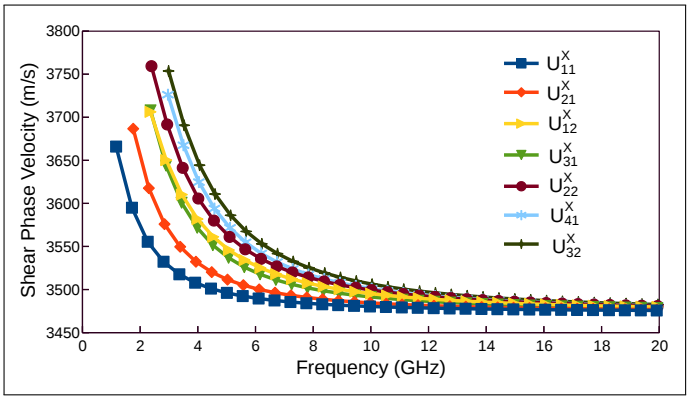

Fig. 2. Variations of the phase velocities with the acoustic frequencies for the transverse modes.

Due to higher doping concentration (10% in this case) of Ge, the acoustic index of the core is increased sufficiently and thus this waveguide supports higher order longitudinal and transverse acoustic modes. Variations of the phase velocities with the acoustic frequency for several transverse modes are shown in Fig. 2. When the frequency is reduced, the phase velocities of the different transverse modes gradually increase. However, at a lower frequency this change is rapid as the modes reach their cut-off conditions and their phase velocities approach those of the cladding velocities, V_{SC}, and beyond that no acoustic mode is guided. It can be noted that the effective cut-off frequency of a higher order mode appears at a higher frequency. The variation of the phase velocity of the fundamental transverse mode, U_{11}^X, is shown by a blue line with square. The higher order longitudinal modes U_{21}^X and U_{12}^X are distinct and are depicted by red and yellow solid lines, with diamond and rightward arrow, respectively. They were different as the height (H) and width (W) of the guide were not equal. In case of H = W, they would have the same modal solution and it would be impossible to isolate these degenerate modes. This guide also supports two near degenerate fundamental transverse modes U_{11}^X and U_{11}^Y, but however, as the symmetry conditions were exploited, these two modes were isolated (as they require different combinations of the symmetry walls).

The displacement vector profiles of the fundamental transverse U_{11}^X acoustic mode are shown in Fig. 3. It can be observed that for any transverse acoustic U_{mn}^X mode with a dominant U_X component, have half sine-wave spatial variation of (m, n), but its non-dominant U_Y and U_Z components have spatial variations of (m+1, n+1) and (m+1, n), respectively.

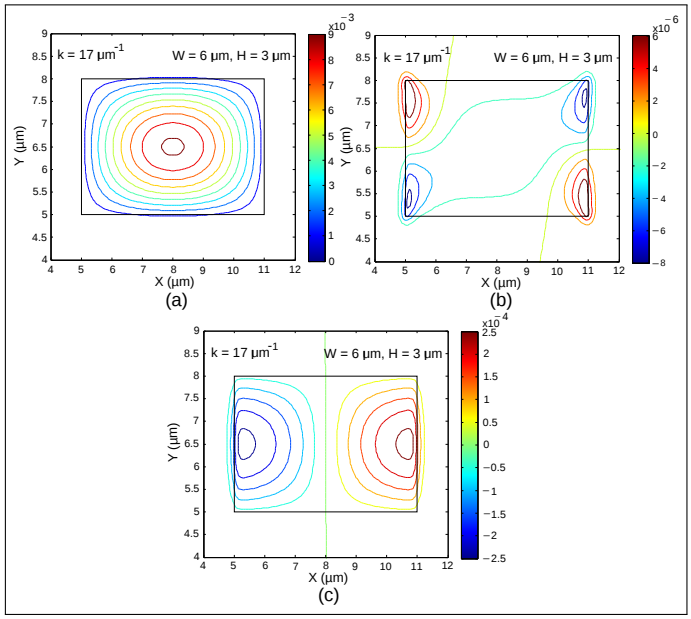

Fig. 3. Displacement vector profiles (a) U_X, (b) U_Y and (c) U_Z of the fundamental transverse U_{11}^X acoustic mode.

This waveguide can also guide longitudinal acoustic modes as the cladding longitudinal velocity is also higher than that of the core. The variations of the phase velocities of the fundamental and higher order longitudinal modes with the frequency are shown in Fig. 4. When frequency is decreased gradually, the velocities of the modes increase from near core velocity to cladding longitudinal wave velocity until they reaches to their cut-off when changes are rapid. The variations of the phase velocities of the U_{21}^Z and U_{12}^Z modes are shown by a red and a yellow lines, with diamond and rightward arrow, respectively and they are distinct. It can be observed that the red line lies below the yellow line for the whole range of the acoustic frequency considered here as the guide width was larger than the height. Here it can also be observed that a higher order mode reaches its cut-off at a higher frequency.

It was observed that the spatial variations of the displacement vector profiles of the longitudinal acoustic modes are different from those of the transverse modes. The dominant and non-dominant displacement vector profiles of the fundamental longitudinal, U_{11}^Z mode are shown in Fig. 5. It can be observed that its U_Z profile has one (m = 1) half-sine variation along the x and similarly one (n = 1) half-sine variation along the y-directions. On the other hand, the U_X profile of this U_{11}^Z mode has one additional spatial variation along the x-direction (m = 2) and

its U_Y profile has one additional variation along the y-direction (n = 2). For a general U^Z_{mn} mode, its dominant component U_Z has (m, n) spatial variations; however its non-dominant U_X and U_Y components have (m+1, n) and (m, n+1) spatial variations, respectively.

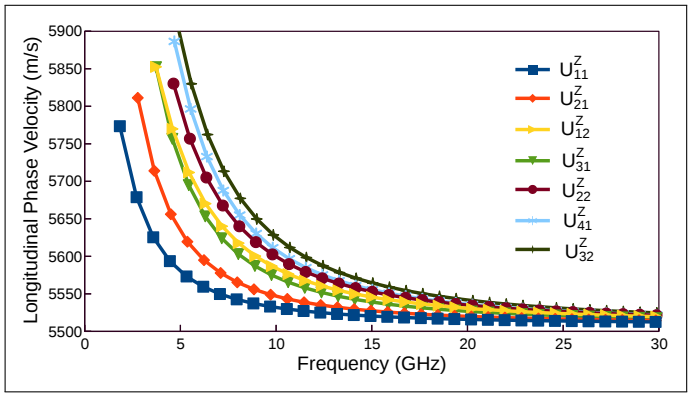

Fig. 4. Variations of the phase velocities with the acoustic frequencies for the longitudinal modes.

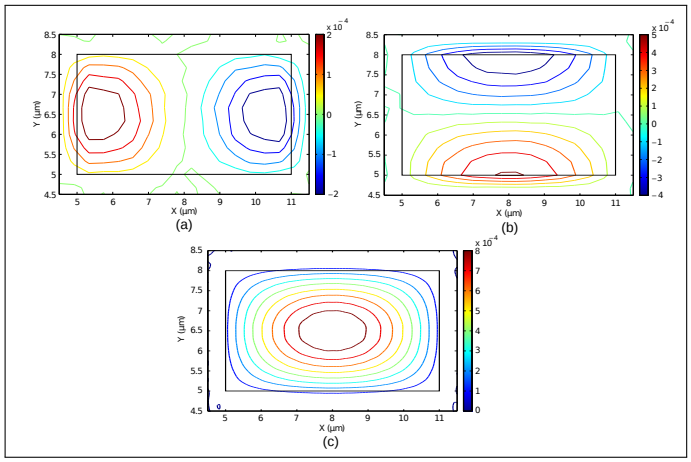

Fig. 5. Displacement vector profiles (a) U_X, (b) U_Y and (c) U_Z of the U^Z_{11} acoustic mode.

Modal solutions of the optical waves in silica planar waveguide, for a wavelength λ_o = 1550 nm, are obtained by using a full-vectorial **H**-field formulation [15]. Here refractive indices of core and cladding are taken as 1.459 and 1.444, respectively. Both quasi-TE and quasi-TM modes can exist in this waveguide, but they have similar propagation constants and the profiles of their dominant **H**-fields are also similar. In this paper the interaction of the transverse and longitudinal acoustic modes with the fundamental quasi-TE, H^Y_{11} mode are studied. At first the effect of waveguide dimensions on the modal properties of both optical and acoustic modes are studied. However, as in most of the planar optical waveguides often the guide widths are easily controlled by mask design for a given planar thickness, so here only the effect of width is shown. The variations of the effective index (n_{eff}) and effective area (A_{eff}) of the H^Y_{11} mode with the guide width (W) are presented in Fig. 6 by a dashed blue and a red solid lines, respectively. The mode size area or the effective area (A_{eff}) can be given [23] by,

$$A_{eff} = \frac{\left(\int\int_\Omega |E_t|^2 dxdy\right)^2}{\int\int_\Omega |E_t|^4 dxdy} \qquad \textbf{(10)}$$

here E_t represents the transverse electric field vector and the surface integration is carried out over the whole cross section, Ω, of the waveguide.

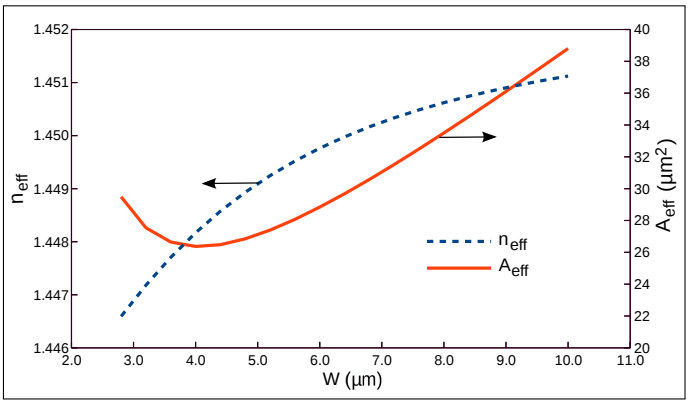

Fig. 6. Variations of the n_{eff} and A_{eff} of the H^Y_{11} mode with the guide width, W.

It can be observed that as the waveguide width, W, is reduced, initially the effective area, A_{eff}, reduces and reaches its minimum value of 26.37 μm^2 when W = 4 μm. However, if W is reduced further, its effective area increases rapidly as the optical mode approaches its effective cut-off condition. Moreover, when the guide width reduces, n_{eff} gradually falls from the effective index of a slab with height (H) 3 μm, to the cladding refractive index value. Below a width of 4 μm, the optical mode spreads out before reaching its cut-off. It should be noted that as modes spreads out more from the core into the cladding, the scattering loss at the core-cladding interface, leakage loss, and bending loss (if bent), increase rapidly and it cannot be used as an effective waveguide.

In a way similar to the optical mode, the acoustic U_X vector profile of the acoustic U^X_{11} mode also varies with the waveguide width. The variations of the spotsizes along the x and y directions with the width, W, for the U_X profile, when propagation constant k = 12 μm^{-1}, are shown in Fig. 7. In this work, the acoustic spotsize is considered as the distance along the x and y-axes where the acoustic displacement profile is approximately equal to the $1/e$ times of the maximum value of a given acoustic mode. Here, the guide height is kept constant at H = 3 μm. The spotsize, σ_X, denoted by a blue dashed line, decreases as the width is decreased but near the effective cut-off this value start increasing. The spotsize, σ_Y, remains almost constant (as the height was kept constant) as guide width decreases but only near the cut-off, where the spotsize, σ_Y, increases.

The frequency and the intensity of the backward flow of the pump signal, termed the Stokes wave, depends essentially on the phase and momentum matching and the overlap between, respectively, the acoustic and optical waves. This phenomenon is further stimulated when interference occurs between the Stokes wave and the laser signal and this strengthens the acoustic wave through electrostriction. Since the scattered light undergoes a Doppler frequency shift, the SBS frequency, f_{SBS}, depends on the acoustic velocity and this can be calculated [1, 24] from,

$$f_{SBS} = \frac{2n_{eff}v}{\lambda_o} \qquad \textbf{(11)}$$

here, v is the acoustic velocity, λ_o is optical wavelength and n_{eff} is the effective index of the optical mode.

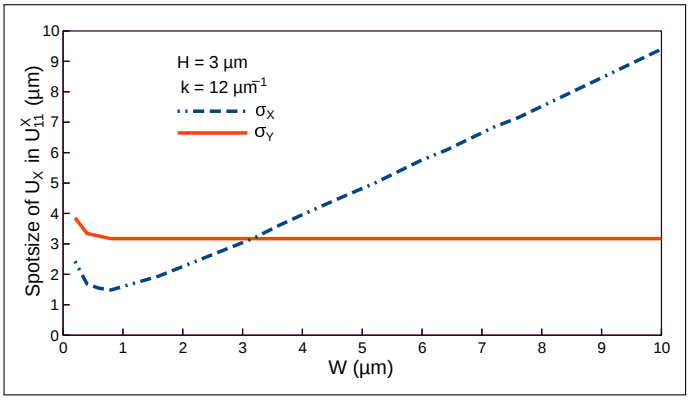

Fig. 7. Variation of spotsizes of the U_X profile for the U_{11}^X mode with the width, W.

The dominant H_Y field profile of the quasi-TE mode has similar profile to that of the dominant U_X, U_Y and U_Z vector fields of the fundamental U_{11}^X, U_{11}^Y and U_{11}^Z acoustic modes, respectively. The normalized amplitude variations of these profiles along x-axis for W = 6 μm, H = 3 μm, λ_o = 1.55 μm and k = 11.75 μm^{-1} are shown in Fig. 8. The k value selected here is the required propagation constant of the acoustic modes phase matched to quasi-TE optical mode at λ_o = 1.55 μm. The U_X, U_Y and U_Z displacement vector profiles are almost identical and they were difficult to identify individually. The H_Y profile of the quasi-TE mode at λ_o = 1550 nm is also shown by a solid black line in Fig. 8, which spreads more into the cladding region, compared to the acoustic mode profiles for this specific case.

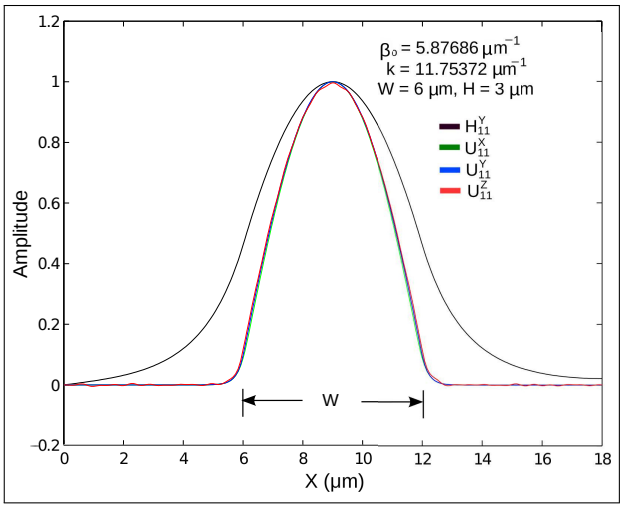

Fig. 8. Normalized field and displacement vector profiles along the x-axis.

Next, the overlap between the fundamental longitudinal, U_{11}^Z acoustic mode and the H_{11}^Y optical mode is calculated when varying the waveguide width and this is shown in Fig. 9 by the dashed blue line. When the guide width increases, the overlap increases more prominently at the beginning then reaches near to its maximum overlap value, after which it increases slowly. The overlap found at 10 μm width was 94%.

As expected, the overlap of U_Z displacement vector of the U_{21}^Z mode (with odd profile) with the H_Y field of H_{11}^Y mode (with even profile) was calculated to be zero and not shown here.

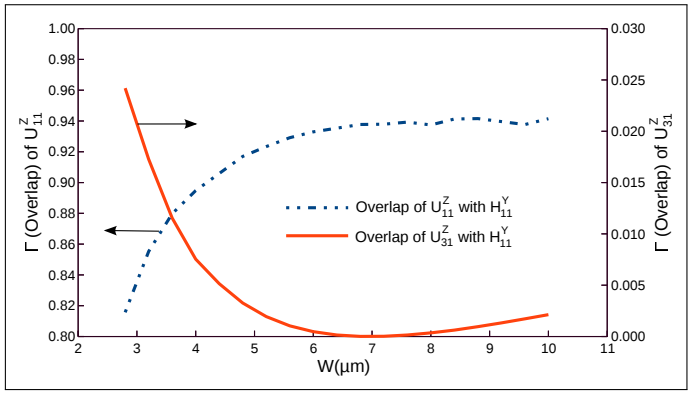

Fig. 9. Overlap of H_Y field of the H_{11}^Y mode with the U_Z displacement vector of the U_{11}^Z and U_{31}^Z modes with W.

Following this, the overlaps of the dominant H_{11}^Y optical field with the higher order longitudinal U_{31}^Z acoustic mode but with symmetric (or even) displacement profiles is also determined and the overlap variation with the width is shown by a solid (red) line in Fig. 9. With the increase in the guide width, as the mode profile becomes more confined, the overlap decreases. It can be noted that, for this mode, the maximum overlap was found to be near 2.5%, at the lower guide width.

After determining the propagation constant, β_o, of the interacting H_{11}^Y mode, the propagation constant of the acoustic mode can be found using Eq. (8). The corresponding phase velocity, v, of the acoustic mode can then be determined and thus Eq. (11) can yield the SBS frequency. In Fig. 10, the SBS frequency shifts with the guide width for the fundamental longitudinal acoustic mode, U_{11}^Z, and the third order longitudinal, U_{31}^Z mode are shown by a solid red and a dashed blue lines, respectively. Here the dashed blue line falls with the increasing guide width, whereas the solid red line reaches its minimum near the 4 μm width and rises again with the increase of width, although this variation is, very small, when compared to the variation for the higher order longitudinal U_{31}^Z mode.

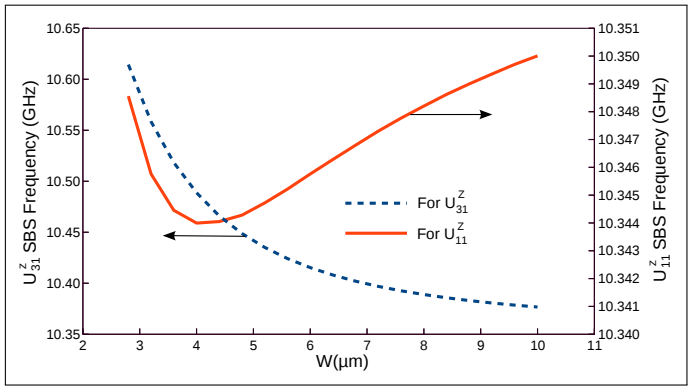

Fig. 10. SBS frequency shifts for the U_{11}^Z and U_{31}^Z modes with waveguide width.

The axial displacement of the material for the longitudinal mode causes a z-dependent density variation which produces an optical grating and influences the propagation of optical modes. Alternatively, if the transverse movement of materials is constant then it can cause bending of the guide. However, as the material displacement in the transverse plane is not constant [as

shown in Fig. 3(a)], this would also cause a density variation along the transverse plane. This would create a refractive index gradient with an axial periodicity related to its wavelength and this may also interact with the optical modes. Recently, it has been reported [25] that the gain peak due to a transfer mode can be larger than that of a longitudinal mode, where the numerical results were verified experimentally and in the numerical analysis molecular displacements were considered rather than density variation, as done in this work.

As the field profiles of both the dominating fields of the acoustic transverse modes are similar to the H_Y field profile of the H_{11}^Y mode, their overlap was found to be quite high. Such overlaps can be calculated by using the normalized form of Eq. (9) and shown in Fig. 11. It can be observed from this figure that the overlap of the U_X field profile of dominant fundamental acoustic transverse mode U_{11}^X with the H_Y field profile of quasi-TE mode becomes higher when the guide width is wider. At a larger guide width, the U_X field profile of U_{11}^X becomes more elongated and this profile becomes closer in shape to the optical profile. Furthermore, it can be noted that the change of the overlap between the U_Y displacement profile of the U_{11}^Y mode and H_Y field profile with the guide width is slightly less than the overlap for the U_{11}^X mode as shown here and both of them are considerably lower than that of the U_{11}^Z mode, which was shown in Fig. 9.

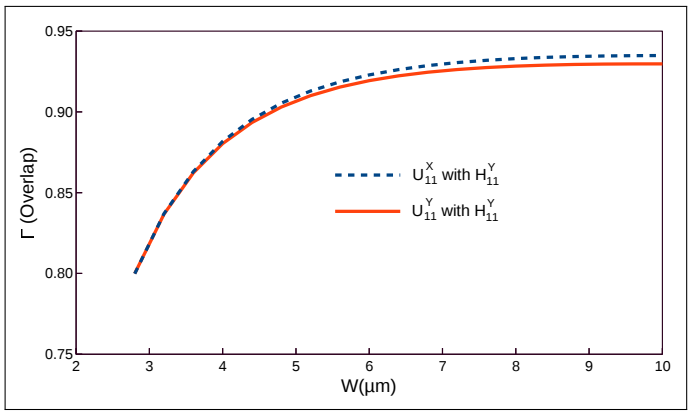

Fig. 11. Variations of the H_Y field overlap of the H_{11}^Y mode with the U_{11}^X and U_{11}^Y modes with the width.

Figure 12 shows the value of f_{SBS} for the both fundamental acoustic U_{11}^X and U_{11}^Y transverse modes. The SBS frequency shift for the U_{11}^X mode shown by a dashed blue line in Fig. 12 is slightly lower than the SBS frequency shift denoted by red solid line for the U_{11}^Y mode. When the width increases from 2.8 μm to 10 μm, its optical effective index increases by 0.266%, while its phase matched acoustic velocity reduces by 0.337%. However, as the dispersion curves are not linear, this yield a minimum SBS frequency shift between 4-5 μm. In general, the total ranges of variation of the values of f_{SBS} for both the fundamental transverse modes are quite small (as the numerical values of the changes are only seen in the third digit after the decimal point). It can be noted that for any existing optical mode, when the guide width (W) increases the optical propagation constant (β_o) also increases. As β_o increases, to maintain the phase matching, the acoustic propagation constant (k) also increases according to Eq. (8). Moreover, for any given waveguide the acoustic frequency increases with the incrementing of k. However, as the width also increases, due to these cumulative variations the result is the profile of the SBS frequency with the width which is shown in Fig. 12. The SBS frequencies shown here are lower compared to those for the longitudinal modes, shown in Fig. 9, as the shear velocity of the doped SiO_2 was lower than that of the longitudinal velocity in the same material.

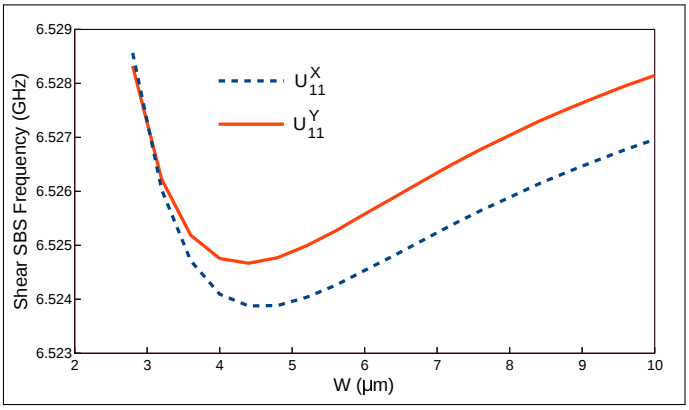

Fig. 12. SBS Frequency shift with guide width.

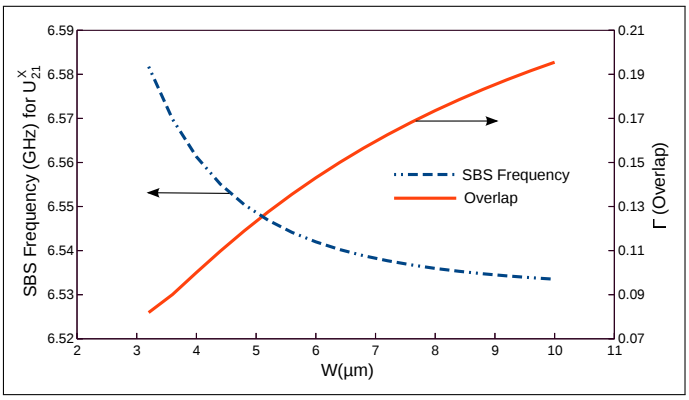

Fig. 13. SBS frequency and overlap for the U_Z component of the U_{21}^X mode with varying guide width.

As the dominant H_Y field profile of the H_{11}^Y mode and the dominant displacement profiles of the fundamental acoustic modes are similar, their overlaps would be significant, as shown in Fig. 11. On the other hand, the overlap of this H_Y field profile of the quasi-TE mode with the non-dominant displacement vector profiles of the fundamental acoustic longitudinal and transverse modes, which have odd symmetry, will cancel out and the resulting acousto-optical interactions would be negligible. However, it is expected that the maximum overlap of the H_Y field profile with the dominant U_X profile of the U_{31}^X mode will be small, and this was observed to be around 3.5% (but is not shown here). However, it should be noted that although the overlap of U_X profile of the U_{21}^X mode with the optical field is zero as the former has odd symmetry, however the non-dominant U_Z profile of this mode may have a considerable overlap, as this displacement vector profile has an even symmetry. The variations of the overlap of U_Z field profile of U_{21}^X mode with the width is shown in Fig. 13 by a red solid line, where it increases along with the guide width. It is observed that the non-dominant U_Z field profile of U_{21}^X mode has a near 20% overlap with the dominant profile of the quasi-TE mode and this is much higher than the overlap of the dominant displacement vector of the higher order mode. The SBS frequency shift for this transverse mode is shown by the dashed blue line, and this drops with the

increasing width. Previously it was also observed, in Fig. 10, that for the U_{31}^{Z} longitudinal mode the value of f_{SBS} also reduces with the width, but had higher values as its longitudinal and shear velocities were higher.

Another important parameter, the peak Brillouin gain, g_B, can be calculated according to [26]:

$$g_B = \Gamma \frac{4\pi n^8 p_{12}^2}{\lambda_o^3 c \rho f_{SBS} \triangle v_B} \tag{12}$$

where, Γ is acousto-optical overlap, n is refractive index of the core, p_{12} is elasto-optic coefficient, λ_o is wavelength of the pump, ρ is density of silica, f_{SBS} is Brillouin frequency shift, c is speed of light in free space and $\triangle v_B$ is the Brillouin gain linewidth.

Before calculation of the Brillouin gain coefficients, it is important to estimate these parameters for 10% Ge-doped silica waveguide. The Brillouin gain linewidth, $\triangle v_B$ is related to the lifetime (T_B) of phonon, i.e. the quanta of acoustic vibration, in the material. It is the full-width at half-maximum (FWHM) of the Lorentzian gain profile [27]. The spectral width can be related to the damping time of acoustic wave by [28] $\triangle v_B = \frac{1}{\pi T_B}$. For 10% Ge-doped silica if the acoustic wave damping time is considered as T_B = 6.469 ns [29], then we have, $\triangle v_B$ = 49.205 MHz. For such a structure, often it is assumed that $\triangle v_B$ to be equal for all acoustic modes and is assumed to be around 30-50 MHz for all silica based fibers [27]. The value of 49.205 MHz is used as Brillouin gain linewidth for all the acoustic modes of this structure.

The another important parameter is the p_{12}, the elasto-optic coefficient. Its value for 3.6% Ge-doped silica with refractive index, n = 1.4492, is 0.27 [30]. This value was considered for optical wavelength λ_o = 1550 nm. For silica, the value of p_{12} = 0.286 [26]. It is well known that for binary SiO_2 - GeO_2 glass the refractive index has a nearly linear relationship with molar composition. It was also reported [31] that for aluminosilicate optical fiber p_{12} shows a linear relation with the concentration of alumina in silica. For the un-doped and 3.6% Ge-doped silica the p_{12} values have been reported as of 0.286 and 0.27, respectively, and from these values, the p_{12} value for 10% Ge-doped silica can be extrapolated as 0.2416.

At the phase matched condition Γ and f_{SBS} can be calculated from Eqs. (9) and (11), respectively as shown earlier. Subsequently using Eq. (12), the Brillouin gain coefficient for the 10% Ge-doped silica waveguide can also be calculated for fundamental and higher order acoustic waves. Table 1 provides overlaps, Brillouin gain coefficients, SBS frequencies and corresponding acoustic velocities of the transverse and longitudinal acoustic modes at the phase matched k = 11.75372 μm^{-1}. Among the fundamental and higher order acoustic transverse and longitudinal modes, which have considerable contributions in Brillouin gain spectrum are only considered here. Other acoustic modes for being odd symmetric will either cancel out or may have negligible gain.

The frequency dependent Brillouin gain, $g_B(f)$, for an individual mode has a Lorentzian spectral profile and can be given as [24]:

$$g_B(f) = g_B \frac{(\triangle v_B/2)^2}{(f - f_{SBS})^2 + (\triangle v_B/2)^2} \tag{13}$$

where, g_B is the Brillouin gain peak, f_{SBS} is Brillouin frequency shift, and $\triangle v_B$ is Brillouin gain linewidth.

The Brillouin gain spectrum (BGS) for 10% Ge-dopoed silica are obtained by considering the gain spectra due to various acoustic modes are statistically independent [27]. The BGS for the 10% Ge-doped silica waveguide in between 6 to 10.5 GHz is shown in Fig. 14. There are two significant peaks observed, the fist peak is the contribution of U_{11}^{X} and U_{11}^{Y} modes and the second peak caused by U_{11}^{Z} and U_{21}^{Z} modes. Due to comparatively larger value of the linewidth, the peaks of two fundamental transverse U_{11}^{X} and U_{11}^{Y} modes are not distinguishable. It can also be noted that in this case, the gain peak for the transverse mode is higher than that of the longitudinal mode, similar as reported earlier [25].

Table 1. Overlaps and Brillouin gain coefficients for transverse and longitudinal fundamental and higher order acoustic modes

Mode	Component	f_{SBS} (GHz)	Overlap (Γ)	g_B (m/W)
U_{11}^{X}	U^X	6.524534	0.922884	1.6554×10^{-11}
U_{11}^{Y}	U^Y	6.525579	0.9193147	1.6487×10^{-11}
U_{11}^{Z}	U^Z	10.345761	0.9329418	1.0554×10^{-11}
U_{21}^{X}	U^Z	6.541982	0.143052446	2.5591×10^{-12}
U_{21}^{Z}	U^X	10.371924	0.1459039	1.6463×10^{-12}
U_{31}^{X}	U^X	6.570862	0.00149854	2.6690×10^{-14}
U_{31}^{Y}	U^Y	6.570515	0.000800863	1.4065×10^{-14}
U_{31}^{Z}	U^Z	10.41532	0.000471823	5.3017×10^{-15}

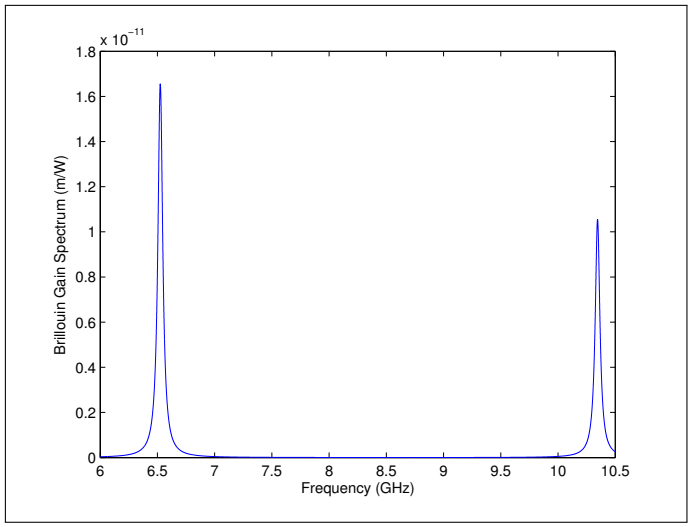

Fig. 14. Brillouin gain spectrum of 10% Ge-doped silica waveguide between 6 GHz to 10.5 GHz.

4. CONCLUSION

Modal solutions of the fundamental and higher order longitudinal and transverse acoustic modes of a Ge-doped planar silica waveguide are presented, obtained by using a full-vectorial finite element method. The dominant and non-dominant displacement vector profiles of both the transverse and longitudinal acoustic modes are presented here. Here existing symmetries of the waveguide have been exploited, not only to improve the solution accuracy but also to avoid degeneration of some of these modes. An **H**-field based full-vectorial program has also been used to find the optical modes of this waveguide.

Subsequently, as the same finite element mesh topology is used for both the acoustic and optical modal solutions, the overlap between the acoustic and optical modes were obtained accurately and more efficiently. Variations of the f_{SBS} and overlaps are shown for the fundamental and higher order longitudinal and transverse acoustic modes with the fundamental quasi-TE optical mode.

It was observed that all the acoustic modes are hybrid in nature with all the three components of the displacement vectors. It was also shown that the non-dominant displacement vectors have smaller magnitudes but also have higher order spatial variations. Further, it was observed that for the fundamental acoustic modes (for both longitudinal and transverse modes) the overlap of the non-dominant displacement vectors (being anti-symmetric) with the dominant H_Y profile (of the fundamental quasi-TE mode) is zero.

For the first time, it was also shown here that the non-dominant displacement vector of higher order acoustic modes can have a symmetric profile and also a considerably higher overlap with the optical mode. It has also been shown in this work that although the overlap of the dominant displacement vector of a mode with odd spatial variations was zero with the fundamental quasi-TE mode, but the overlap of its non-dominant displacement vector was significantly high and cannot be ignored.

The Brillouin gain coefficients of some transverse and longitudinal modes are also calculated and presented. Along with these the Brillouin gain spectrum from 6 GHz to 10.5 GHz is presented, which shows larger two peaks around 6.524534 GHz and 10.345761 GHz.

A rigorous study of light-sound interactions in optical waveguide can be useful in the development of novel SBS sensors or in the design of optical waveguide to deliver high power. Thus the research presented has shown that to study light-sound interaction in an effective way, the use of full-vectorial acoustic and optical modal approaches are necessary.

REFERENCES

1. G. P. Agrawal, *Nonlinear Fiber Optics*, 5th ed. (Academic Press, 2013).
2. K. Park and Y. Jeong, "A quasi-mode interpretation of acoustic radiation modes for analyzing Brillouin gain spectra of acoustically antiguiding optical fibers," *Opt. Exp.* **22**(7), 7932–7946 (Apr. 2014).
3. B. A. Auld, *Acoustic Fields and Waves in Solids*, vol. I (John Wiley & Sons, 1973).
4. P. Dainese, P. St. J. Russell, N. Joly, J. C. Knight, G. S. Wiederhecker, H. L. Fragnito, V. Laude and A. Khelif, "Stimulated Brillouin scattering from multi-GHz-guided acoustic phonons in nanostructured photonic crystal fibers," *Nature Phys.* **2**, 388–392 (Jun. 2006).
5. R. N. Thurston, "Elastic waves in rods and clad rods," *J. Acous. Soc. Am.* **64**(1), 1–37 (Jul. 1978).
6. A. Saffaai-Jazi, "Acoustic modes in optical fiber like waveguides," *IEEE Trans. Ultrason. Ferroelectr. Freq. Control* **35**(5), 619–627 (Sep. 1988).
7. B. M. A. Rahman, M. M. Rahman, S. Sriratanavaree, N. Kejalakshmy, and K. T. V. Grattan, "Rigorous analysis of the transverse acoustic modes in optical waveguide by exploiting their structural symmetry," *App. Opt.* **53**(29), 6797–6803 (Oct. 2014).
8. B. M. A. Rahman and A. Agrawal, *Finite Element Modelling Methods for Photonics* (Artech House, 2013).
9. M. Koshiba, S. Mitobe, and M. Suzuki, "Finite-element solution of periodic waveguides for acoustic waves," *IEEE Trans. Ultrason. Ferroelectr. Freq. Control* **UFFC-34**(4), 472–477 (Jul. 1987).
10. P. E. Lagasse, "Higher-order finite-element analysis of topographic guides supporting elastic surface waves," *J. Acoust. Soc. Am.* **53**(4), 1116–1122 (Jan. 1973).
11. G. O. Stone, "High-order finite elements for inhomogeneous acoustic guiding structures," *IEEE Trans. Microw. Theory Tech.* **MTT-21**(8), 538–542 (Aug. 1973).
12. S. Sriratanavaree, B. M. A. Rahman, D. M. H. Leung, N. Kejalakshmy, and K. T. V. Grattan, "Rigorous characterization of acoustic-optical interactions in silicon slot waveguides by full-vectorial finite element method," *Opt. Exp.* **22**(8), 9528–9536 (Apr. 2014).
13. B. Ward and J. Spring,"Finite element analysis of Brillouin gain in SBS-suppressing optical fibers with non-uniform acoustic velocity profiles," *Opt. Exp.* **17**(18), 15685–15699 (Aug. 2009).
14. O. C. Zienkiewicz, R. L. Taylor, and J. Z. Zhu, *The Finite Element Method: Its Basis and Fundamentals*, 7th ed. (Butterworth-Heinemann, 2013).
15. B. M. A. Rahman and J. B. Davies, "Finite element solution of integrated optical waveguides," *J. Lightwave Technol.* **LT-2**(5), 682–688 (Oct. 1984).
16. R. W. Boyd, *Nonlinear Optics*, 3rd ed. (Academic Press, 2008).
17. P. T. Rakich, C. Reinke, R. Camacho, P. Davids, and Z. Wang,"Giant enhancement of stimulated Brillouin scattering in the subwavelength limit," *Phys. Rev. X* **2**, 011008(1–15) (Jan. 2012).
18. L. Tartara, C. Codemard, J. -N. Maran, R. Cherif and M. Zghal, "Full modal analysis of the Brillouin gain spectrum of an optical fiber," *Opt. Comm.* **282**(12), 2431–2436 (Jun. 2009).
19. R. Pant, C. G. Poulton, D. -Y. Choi, H. Mcfarlane, S. Hile, E. Li, L. Thevenaz, B. L. -Davies, S. J. Madden and B. J. Eggleton,"On-chip stimulated Brillouin scattering," *Opt. Exp.* **19**(9), 8285–8290 (Apr. 2011).
20. M. -J. Li, X. Chen, J. Wang, S. Gray, A. Liu, J. A. Demeritt, A. B. Ruffin, A. M. Crowley, D. T. Walton, and L. A. Zenteno, "Al-Ge co-doped large mode area fiber with high SBS threshold," *Opt. Lett.* **15**(13), 8290–8299 (Jun. 2007).
21. C. K. Jen, A. Saffaai-Jazi, and G. W. Farnell, "Leaky modes in weakly guiding fiber acoustic waveguides," *IEEE Tran. Ultrason. Ferroelectr. Freq. Control* **UFFC-33**(6), 619–627 (Nov. 1986).
22. P. D. Dragic, "The acoustic velocity of Ge-doped silica fibers: A comparison of two models," *Int. J. App. Glass Sci.* **1**(3), 330–337 (Aug. 2010).
23. M. Uthman, B. M. A. Rahman, N. Kejalakshmy, A. Agrawal, H. Abana, and K. T. V. Grattan, "Stabilized large mode area in tapered photonic crystal fiber for stable coupling," *IEEE Photon. J.* **4**(2), 340–349 (Apr. 2012).
24. M. Nikles, L. Thevenaz, and P. A. Robert, "Brillouin gain spectrum characterization in single-mode optical fibers," *J. Lightwave Tech.* **15**(10), 1842–1851 (Oct. 1997).
25. J. -C. Beugnot, S. Lebrun, G. Pauliat, H. Maillotte, V. Laude and T. Sylvestre, "Brilllouin light scattering from surface acoustic waves in a subwavelength-diameter optical fiber," *Nat. Comm.* **5**(5242), 1–6 (Oct. 2014).
26. B. J. Eggleton, C. G. Poulton and R. Pant, "Inducing and harnessing stimulated Brillouin scattering in photonic integrated circuits," *Adv. Opt. Phot.* **5**, 536–587 (Dec. 2013).
27. S. Dasgupta, F. Poletti, S. Liu, P. Petropoulos, D. J. Richardson, L. Grüner-Nielsen and S. Herstrom, "Modelling Brillouin gain spectrum of solid and microstructured optical fibers using a finite element method," *J. Lightwave Tech.* **29**(1), 22–30 (Jan. 2011).
28. K. Ogusu and H. Li, "Brillouin-gain coefficient of chalcogenide glasses," *J. Opt. Soc. Am. B* **21**(7), 1302–1304 (Jul. 2004).
29. Y. Koyamada, S. Sato, S. Nakamura, H. Sotobayashi and W. Chujo, "Simulating and designing Brillouin gain spectrum in single-mode fibers," *J. Lightwave Tech.* **22**(2), 631–639 (Feb. 2004).
30. J. -C. Beugnot and V. Laude, "Electrostriction and guidance of acoustic phonons in optical fibers," *Phys. Rev. B* **86**(22), 224304 (Dec. 2012).
31. P. D. Dragic, J. Ballato, S. Morris and T. Hawkins, "Pockel's coefficient of alumina in aluminosilicate optical fiber," *J. Opt. Soc. Am. B* **30**(2), 244–250 (Feb. 2013).